Topologies of velocity-field stagnation points generated by a single pair of magnets in free-surface electromagnetic experiments

J. M. García de la Cruz[*] and J. C. Vassilicos

Imperial College London, South Kensington Campus, London SW7 2AZ, United Kingdom

L. Rossi

CEA, CEA Saclay, DEN, DANS/DM2S/STMF/LIEFT 91191 Gif-sur-Yvette, France

The velocity fields generated by a static pair of magnets in free-surface electromagnetically forced flows are analyzed for different magnet attitudes, ionic currents, and brine depths. A wide range of laminar velocity fields is obtained despite the forcing simplicity. The velocity fields are classified according to their temporal mean flow topology, which strongly depends on the forcing geometry but barely on its strength, even through the bifurcation to unsteady regimes. The mean flow topology possesses a major influence on the critical Reynolds number Re_c under which the steady velocity fields remain stable. The qualitative comparison of the dependence of Re_c on the topology is in agreement with previous works. The unsteady configurations evidence the advection of smaller flow structures by the largest scales, commonly known as "sweeping."

I. INTRODUCTION

Since Tabeling and co-workers employed an electromagnetic (EM) free-surface experiment to study decaying two-dimensional (2D) turbulence [1], forcing a shallow layer of brine has been a common method to study turbulent and chaotic flows. Some of the works studying turbulence with such a technique focused on freely decaying 2D turbulence [2], scalar mixing in the viscous-convective range [3–5], and Richardson pair dispersion [5–7]. Other works employed the 2D EM apparatus to study chaotic mixing in stretching fields [8–10], symmetry breaking [11], nonperiodicity [12], scalar pattern persistence [13], and different properties of spatiotemporal chaos [14–16]. Such was the relevance of that experimental methodology that numerical works studied properties of 2D flows by modeling the EM free-surface apparatus [17–19]. In addition, there has been a growing number of studies characterizing the possibilities of the EM free-surface experiments themselves [20], developing methods to improve their reliability [21] and delimiting a framework within which they can be used in the study of 2D phenomena [22].

To provide the driven flows with particular properties, previous 2D EM studies have employed magnetic fields such as square lattices [3], parallel linear magnets [16], random distributions [11], compartmentalized arrangements [5], and fractal shapes [23]. It is the intention of this work to characterize the velocity fields obtained with a magnet pair and compare the properties observed in this simple setting with previous results.

Features of 2D flows

The topology of the flows can be characterized by the nature and position of their stagnation points. Stagnation points are classically described as points with zero velocity in the frame where the mean flow is zero [7,24,25]. Stagnation points are also local maxima of the instantaneous curvature of the

trajectories described by fluid elements [16] and, in 2D, those points with a finite Poincaré index [26].

In 2D nondivergent flows, as approximated here, the stagnation points are classified as hyperbolic (HSP) or elliptic (ESP), depending on whether their velocity Jacobian eigenvalues (λ) are real or imaginary. Figure 1 presents sketches of flows around an ESP and a HSP. The reader can refer to [27] for flows around stagnation points in 2D and 3D fields.

In 2D EM experiments with static magnetic configurations, the flow stagnation points remain stable and around their preferred locations up to a critical Reynolds number Re_c, whose value depends on the forcing geometry [16]. Beyond Re_c, the stagnation points move and interact with each other; in particular, ESPs and HSPs annihilate and nucleate in pairs. This happens when two coherent vortices merge or one vortex splits into two, respectively. Similar topological dynamics occurs in 2D inverse cascading turbulence [28].

The current work explores the stagnation point interactions and the dependence of Re_c on the forcing geometry. In addition, a case of larger scales advecting smaller flow structures is presented.

II. APPARATUS AND EXPERIMENTAL PROCEDURE

A shallow layer of a conductive solution is electromagnetically forced using a pair of magnets. Schematics of the electromagnetic tank and magnetic arrangement are presented in Fig. 2, which also defines the coordinate system.

A. Laboratory apparatus

The Lorentz force generated by the ionic current density ($\boldsymbol{J}$) and the magnetic field ($\boldsymbol{B}$), $\boldsymbol{f} \sim \boldsymbol{J} \times \boldsymbol{B}$, drives the brine in the tank [1]. The fluid velocity $\boldsymbol{u}$ is related to this force through the Navier-Stokes equation,

$$\partial\boldsymbol{u}/\partial t + (\boldsymbol{u} \cdot \nabla)\boldsymbol{u} = (\boldsymbol{f} - \nabla p)/\rho + \nu\nabla^2\boldsymbol{u}, \qquad (1)$$

where p is the pressure, ρ is the fluid density, and ν is the fluid kinematic viscosity.

---

[*]marcos@imperial.ac.uk
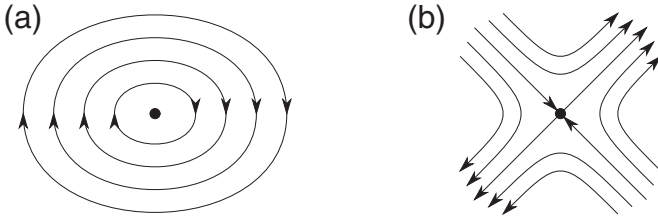
FIG. 1. 2D incompressible stagnation points. Sketches of flows around (a) an elliptic and (b) a hyperbolic stagnation point.

The fluid employed is a solution of NaCl in water at $160 \, \text{g} \, \text{l}^{-1}$, with a density of $1120 \, \text{kg} \, \text{m}^{-3}$, a viscosity of $1 \, \text{mm}^2 \, \text{s}^{-1}$ and a conductivity of $170 \, \text{mS} \, \text{cm}^{-1}$ [29,30]. The magnetic field is generated by two cubic magnets of edge 40 mm with magnetic intensity 0.3 T and placed 40 mm apart. The magnetic field is closed under the magnets by an iron bar. The center of the pair of magnets is fixed. The magnet pair attitude is defined by the angle between the axis bisecting both magnets and the direction perpendicular to the ionic current, as shown in the right-hand side of Fig. 2.

The electric field is generated by one 57 mm row of 20 electrodes centered in each side of the tank. Each electrode is made by a 30 mm 99.95% platinum wire of diameter 250 μm and is separated from the contiguous one by 30 mm. The distance of each row of electrodes from the central working section is larger than ten times the distance between electrodes in a row, so a spatially homogeneous ionic current can be expected in the working section. The ionic current is kept constant with a standard deviation smaller than 0.5% of the nominal value through a home-made controller.

The wall supporting the forced brine is a rectangle of $500 \times 600 \, \text{mm}^2$. The measurement area is a square, centered in that rectangle, of side 440 mm. This area was recorded with a 14-bit digital camera with resolution 2048×2048 pixels (the size recorded by one pixel is $440 \, \text{mm}/2048 \approx 0.215 \, \text{mm}$). The brine free surface extends up to a square of side 600 mm. The wall under the brine has a thickness of 1 mm and its bottom is in direct contact with the magnets. The wall maximum height difference and standard deviation are respectively kept smaller than 0.4 mm and 0.2 mm.

B. Velocity-field acquisition

Particle image velocimetry (PIV) is employed to acquire the velocity fields. The acquisition area is illuminated using white light. Particles of Pliolite DF01 floating on the brine are employed as seeding. The in-house PIV software employed [31] has a numerical uncertainty of 0.05 pixels frames^{-1}. The
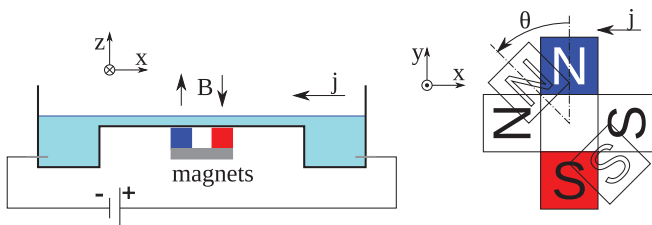
FIG. 2. (Color online) Electromagnetic tank and magnet positioning.
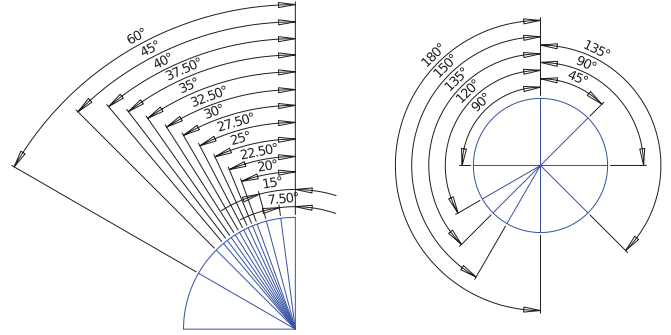
FIG. 3. (Color online) Magnet angles tested.

minimum correlation window size is 16 pixels ≈ 3.4 mm. The PIV mesh covers a square of about 380 mm per side. The nodes in the mesh are 8 pixels apart, for a correlation window overlap of 50%. The particle density is selected to expect around five particles per correlation window. With these parameters more than 95% of the correlation peaks are usually above 80%. The PIV fields obtained are validated using the dynamic mean value operator and the minimum correlation filter [32]. The amount of discarded points was always smaller than 0.2%. Each discarded point was replaced by the surrounding average.

C. Velocity-field statistics

The statistics presented are performed either over a single or over the average of many velocity fields with the same forcing configuration. This average is the nominal field around which unsteady flows oscillate. Spatial statistics are computed in a central circular zone of diameter $\sim$200 mm, five times the size of one magnet. The stagnation points characterizing the velocity fields are found using the Poincaré index of small orbits [26]. The error expected in positioning each stagnation point is smaller than 1 pixel.

D. Experimental scheme

The parameters studied were the magnet angle (θ), the ionic current (I), and the brine depth (h). The nominal depth employed was 6 mm, which was employed to test the magnet angles presented in Fig. 3. The brine depth was varied from 5 to 7 mm for the magnet angles $0°$, $15°$, $30°$, $45°$, $60°$, and $90°$. The ionic current employed was set such that the current density selected was 6.7, 13.3, 26.7, 40, 53.3, or 66.7 A m^{-2}.

The forcing applied contains a second-order rotational antisymmetry. This leads, using Eq. (1), to several symmetries in the mean velocity fields and relations between velocity fields obtained with different angles [22]. In particular, the mean velocity fields obtained with forcing angles θ and $-\theta$ are symmetric to each other with respect to the y axis. Therefore only angles in the range from $0°$ to $180°$ are exhaustively studied and angles between $180°$ and $360°$ are scarcely sampled to test the symmetry. A correlation always above 0.95 is obtained between expected symmetric fields.

Experiments such as those performed here are typically characterized by the Reynolds number Re$_{2D}$, based on the magnet spacing L [3,8,11,16,19,23,33], and the root mean square (rms) velocity U_{rms}. Other length scales employed

TABLE I. Typical U_{rms} in mm/s for different depths and current densities.

Depth (mm)	Current density (A m^{-2})					
	6.7	13.3	26.7	40	53.3	66.7
5	2	3.5	6.5	8.5	10.5	12
6	2	4	7	9	11	12.5
7	3	5	7.5	10	11.5	13

are the cell size [1,2]; U_{rms}/ω_{rms}, where ω_{rms} is the rms vorticity [12]; and the brine depth [23]. Typical values of U_{rms} are presented in Table I. The exact U_{rms} depends on the forcing configuration but mostly remains within 20% of the value presented.

III. VELOCITY-FIELD CHARACTERIZATION

This section describes the time-averaged velocity-field topology in the brine uppermost layer and the unsteady responses presented by some configurations.

A. Free-surface mean velocity-field topology

The mean flow topologies can be classified within the three groups sketched in Fig. 4, top. Representative velocity fields are shown in Fig. 4, bottom.

Configurations with the magnet couple nearly perpendicular to the ionic current [$\sin(\theta) \sim 0$], as exemplified in Fig. 4,

left, present a HSP in the rig center whose streamlines extend up to the boundaries, dividing the domain into four streamline sets. In each set the streamlines surround one of the four existing ESPs.

As $|\sin(\theta)|$ increases, two ESPs approach the central HSP, bending its streamlines until they merge. At such θ a new streamline set, surrounding the approaching ESPs and the HSP, appears. A typical example of such topology is presented in Fig. 4, center.

As the magnets align with the ionic current, the area surrounded by the streamlines around each approaching ESP shrinks and the area occupied by the streamlines around the ESPs and HSP increases. For large values of $|\sin(\theta)|$, the approaching eddies merge (one ESP annihilates with the HSP) leading to the third typical topology, with three ESPs each one surrounded by a streamline set, presented in Fig. 4, right.

For finite distances between the approaching ESPs, d_e, the flow is similar to that obtained for $|\sin(\theta)| \sim 0$ at distances $\ell \ll d_e$ from the center and to the one obtained for $|\sin(\theta)| \sim 1$ for $\ell \gg d_e$. The area of influence of the HSP can therefore be scaled with d_e.

The dependence of the flow topology on the magnet couple angle and ionic current is summarized in Fig. 5(a), which shows the ESP positions for angles varying from 0° to 180°, exemplifies the annihilation of one ESP with a HSP when two vortices merge. Figure 5(c) shows the positions of the ESPs when the ionic current is varied for the angles 0°, 90°, and 180°. Figure presents d_e against the magnet couple angle for different ionic currents. The angle range for which $d_e = 0$ barely depends on Re$_{2D}$ in the range tested. The general
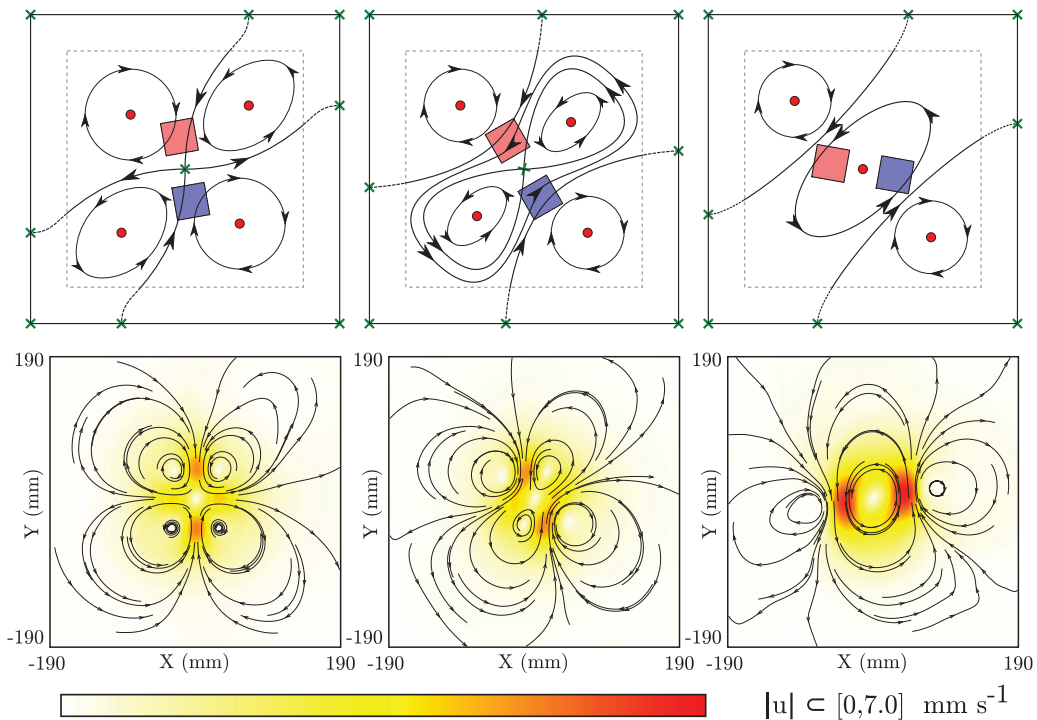
FIG. 4. (Color online) Sketches and examples of the characteristic topologies obtained for increasing θ. Hyperbolic (HSP) and elliptic (ESP) stagnation points are respectively represented by green crosses and red bullets in the sketches. The grey dashed squares in the sketches represent the PIV area, a square of edge 380 mm centered with the magnets. Three examples obtained in the PIV area using 6 mm of brine and 6.7 A m^{-2} at angles 0°, 15°, and 90° are presented.
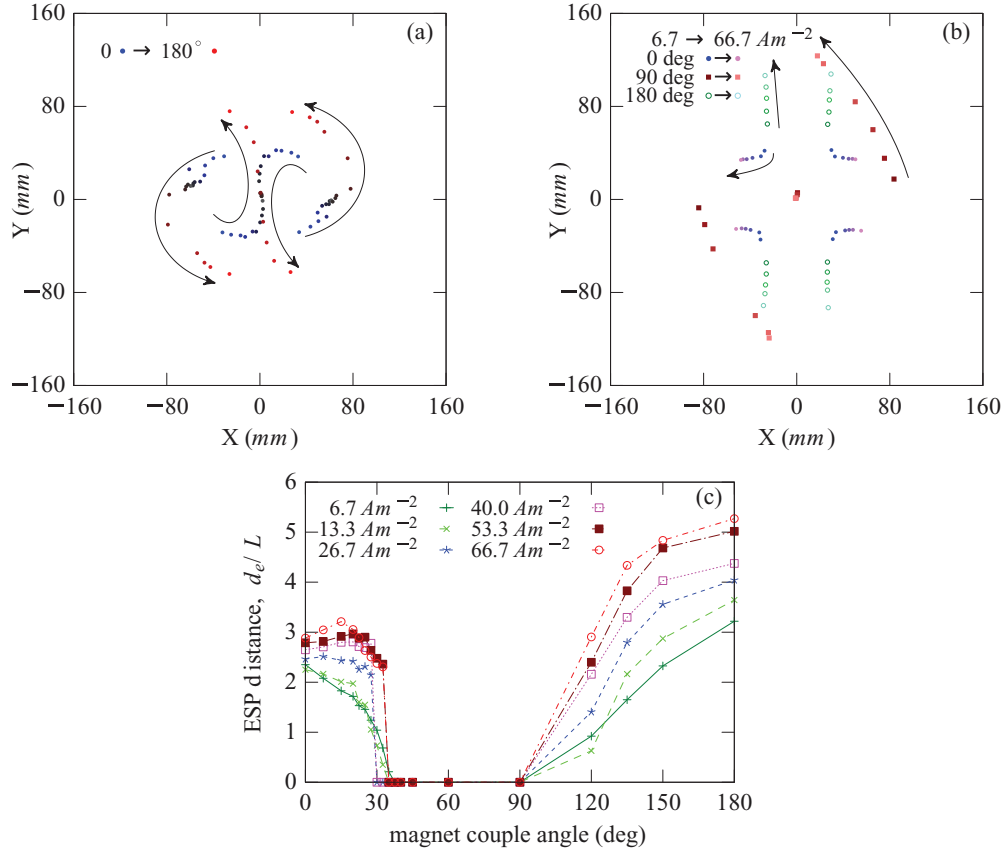
FIG. 5. (Color online) ESP positions. ESPs obtained by varying the magnet angle at 48 mA (a) and by varying the ionic current for angles $0°$, $90°$, and $180°$ (b). Distance d_e between merging vortices for different forcing (c). Brine depth is 6 mm in all cases.

topology of the mean velocity fields presents only three ESPs from around $30°$ to somewhere around $110°$ and one central HSP otherwise. Increasing the ionic current makes the HSP maintain its area of influence for larger angles, but does not appreciably vary the flow topology. The brine depth (not shown in Fig. 5) accentuates the effect of the ionic current and does not affect the topology.

B. Temporal flow dynamics

For constant forcing, flow unsteadiness results from inertia effects, which increase with Re_{2D}. Some of the presented configurations become unsteady and develop periodic oscillatory patterns at moderate Re_{2D}. A Re_{2D} breaking this periodicity was not achieved.

1. Steady flow stability

The flow unsteadiness is characterized by the relative spatial rms of the velocity temporal standard deviation, presented in Figs. 6(a) and 6(b) as a function of the magnet angle, ionic current, and Re_{2D}. The stability of the steady flow depends on the forcing geometry as much as on its strength: for a brine depth of 6 mm, relevant unsteadiness is only present only above 13.3 A m^{-2} ($Re_{2D} \sim 200$) and within the magnet angle range from $30°$ to $120°$. As Re_{2D} becomes supercritical, the flow bifurcates into orbiting around a limit cycle, whose temporal average has the same topology as in the steady regime. There exists a relation between the steady flow stability

and the topology of the averaged velocity field [presented in Fig. 5(c)]: configurations with a central ESP ($d_e = 0$), typically a shear region, become unsteady for lower Re_{2D}. Also, when a central ESP is present, the smallest magnet angles provide higher unsteadiness: as the magnet angle increases, the component of the magnet distance perpendicular to the forcing becomes larger and, as a result, the shear that they directly force is reduced. All this evidences how those forcing configurations favoring shear are more prone to develop unsteadiness than those favoring strain. This result is coherent with previous works showing how the Re_c increases in a 2D EM flow, when changing from magnets arranged in a square lattice to a set of parallel linear magnets, and from this to a random distribution [16]. In effect, each one of these magnet configurations is expected to incrementally force shear with more intensity, either by increasing the forcing coherence (square lattice to parallel linear magnets) or by reducing the minimum length scale between magnets (parallel linear magnets to random arrangement).

Figure 6(c) presents examples of the velocity-field temporal autocorrelations for several ionic currents. In view of their shape, the main oscillatory frequency f_r of the unsteady configurations was measured by adjusting their temporal autocorrelation to $g(t) = M + A \cos(2\pi f_r t)$. Figure 6(d) shows the nearly constant Strouhal number St $= f_r L / U_{\text{rms}}$, with varying Re_{2D}, which reveals how increasing the forcing strength leads to faster flows containing similar structures.
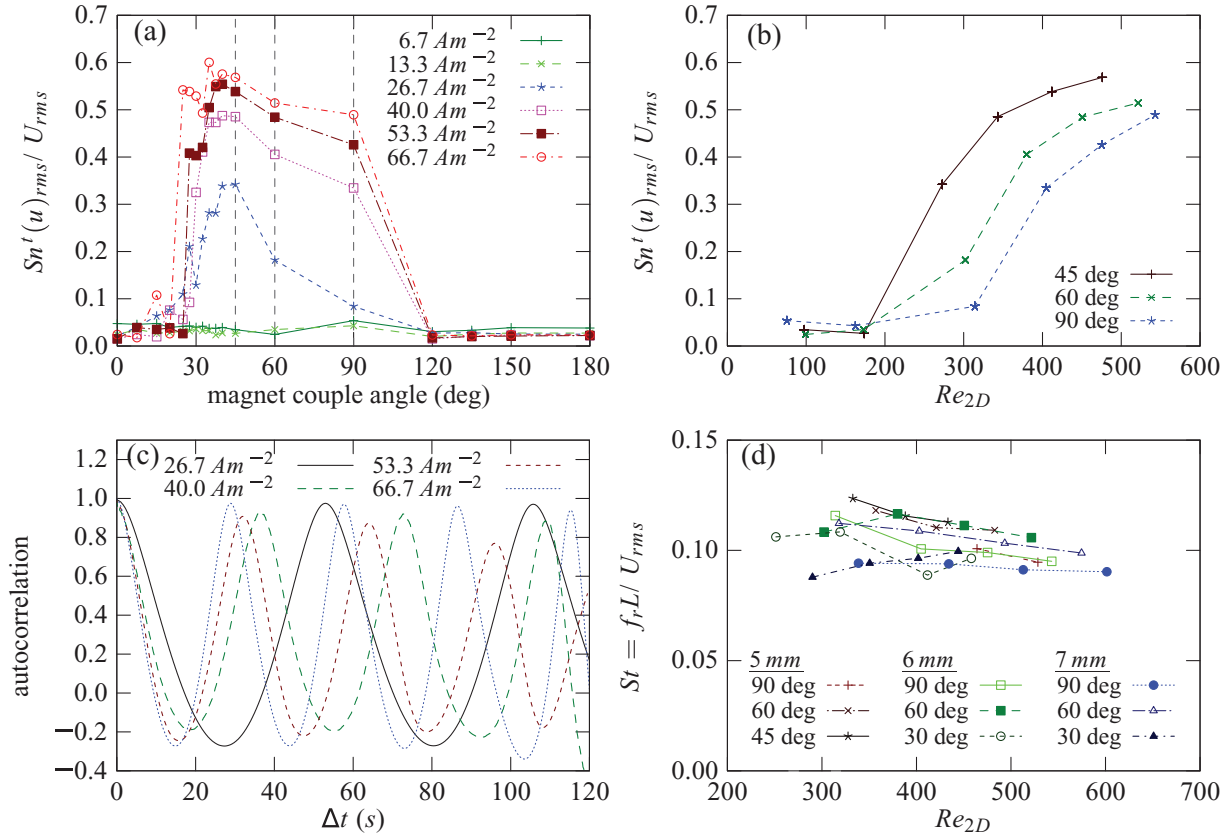
FIG. 6. (Color online) Unsteadiness characterization. Spatial rms of the velocity temporal standard deviation normalized by U_{rms} against angle (a) and Re_{2D} (b); velocity temporal autocorrelation for magnets at $60°$ (c); flow St against Re_{2D} (d).

2. Oscillation, annihilation, and nucleation of stagnation points

The unsteady patterns observed in the experiments are summarized by the examples presented in Fig. 7. This figure shows the history of the flow topology along one period through the locations of its HSPs and ESPs.

For the lowest unsteady magnet angles [Fig. 7(a), $30°$], there are two ESPs orbiting near the magnets and an external cyclic process of nucleation and annihilation of ESPs and HSPs. After the nucleation occurs close to the rig center, the new HSP moves away from the new ESP and towards the original ESP, respectively increasing and reducing the size of their associated vortices. Finally, the original vortex disappears with the annihilation between the HSP and original ESP. The remaining ESP moves outwards and a new nucleation occurs.

For moderate magnet angles [Fig. 7(b), $35°$], the eccentricity of the ESP close orbits increases until they pass through the central HSP. Their associated vortices merge and split while a cyclic annihilation and nucleation process takes place. Also, the external ESP and HSP annihilate with those nucleated on the other side of the rig. The nucleation and annihilation processes occur near each other and within a small part of the oscillatory period. When a vortex arrives in this area, it nucleates and transfers its vorticity to a new small vortex, which follows the track of the original one. Larger magnet angles [Fig. 7(c), $60°$] present one main ESP "clamped" to the rig center and a nucleation and annihilation process like that described for $35°$.

The ESP and HSP path topologies barely depend on Re_{2D} and are mainly affected only by the forcing geometry. The path geometries show a small dependence on Re_{2D}. This small effect of Re_{2D} on the path topologies and geometries is the cause of the nearly constant St with Re_{2D}.

3. Advection of small structures

In unsteady configurations containing a clear hierarchy of scales, $d_e/L \ll 1$, the external smaller eddies are advected by a larger-scale flow. Such a process is reminiscent of the extrapolation of the Taylor hypothesis for different length scales in turbulent flows [34]. This effect, commonly referred to as *sweeping*, is based on the assumption that the smaller structures are independent of the larger ones. In the case reported, the smaller vortices are *swept* with a velocity which depends on the large-scale flow, keeping St constant for different Re_{2D}. The motion of these structures determines the position of the stagnation points; in particular an ESP roughly follows a vortex center (with a small deviation produced by the motion of the vortex itself). Using the hypothesis of statistical independence, the large-scale flow can be considered approximately equal to the temporal mean. For each field, the temporal mean is one of those sketched in Fig. 4 and is defined by the position of its stagnation points. The ESP sweeping cannot be locally defined as in the case of other topological objects such as the zero-acceleration points [28], since the velocity field in it is 0. Nevertheless, observation of the ESP motion in Figs. 7(b) and 7(c) with respect to the position
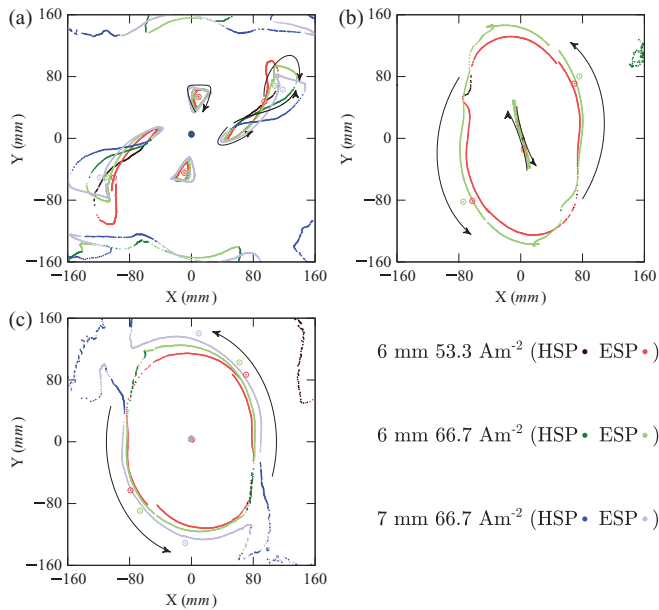
FIG. 7. (Color online) Stagnation point paths for steady forcing. Path followed by HSP and ESP in one period for magnet angles 30° (a), 35° (b), and 60° (c), and several combinations of current and depth. For each configuration, the stagnation points of the mean flow are presented circled.

of the stagnation points of the large-scale flow qualitatively evidences the eddy advection.

IV. CONCLUSIONS

The velocity fields generated by electromagnetically forcing a shallow layer of conductive brine by a pair of magnets with opposite polarity have been analyzed. Several forcing intensities, magnet attitudes, and brine depths were explored. The behavior observed in these forcing configurations can help in understanding the flow response to the more complex magnetic distributions commonly found in the literature.

The velocity fields obtained were classified according to their temporal average topology within three groups in Sec. III A. The forcing geometry possesses a major influence on the mean flow topology while the forcing intensity modifies only its geometry.

The stability of the steady flow was studied in Sec. III B 1. As Re_{2D} is increased the flow becomes unsteady and bifurcates into a limit cycle state. Throughout this process, the flow's temporal average does not vary its topology. The magnet arrangement and therefore the mean flow topology were evidenced as being as relevant for unsteadiness as the Re_{2D}, in agreement with [16]. Forcing geometries favoring shear lead to flows which are more prone to unsteadiness. Understanding what makes flows unsteady at low Re_{2D} could help in specifically designing magnet arrangements with higher tendency to develop chaotic behavior in laminar flows, a desirable feature in mixers.

The evolution of particular unsteady velocity-field topologies was analysed in Sec. III B 3. Smaller eddies were observed to be advected by larger structures when a scale hierarchy was present in a process reminiscent of the sweeping mechanism described in [34].

[1] P. Tabeling, S. Burkhart, O. Cardoso, and H. Willaime, Phys. Rev. Lett. **67**, 3772 (1991).

[2] O. Cardoso, D. Marteau, and P. Tabeling, Phys. Rev. E **49**, 454 (1994).

[3] B. S. Williams, D. Marteau, and J. P. Gollub, Phys. Fluids **9**, 2061 (1997).

[4] M.-C. Jullien, P. Castiglione, and P. Tabeling, Phys. Rev. Lett. **85**, 3636 (2000).

[5] M.-C. Jullien, Phys. Fluids **15**, 2228 (2003).

[6] M.-C. Jullien, J. Paret, and P. Tabeling, Phys. Rev. Lett. **82**, 2872 (1999).

[7] L. Rossi, J. C. Vassilicos, and Y. Hardalupas, Phys. Rev. Lett. **97**, 144501 (2006).

[8] G. A. Voth, G. Haller, and J. P. Gollub, Phys. Rev. Lett. **88**, 254501 (2002).

[9] L. Rossi, D. Doorly, and D. Kustrin, Europhys. Lett. **97**, 14006 (2012).

[10] L. Rossi, D. Doorly, and D. Kustrin, Phys. Fluids **25**, 073604 (2013).

[11] G. A. Voth, T. C. Saint, G. Dobler, and J. P. Gollub, Phys. Fluids **15**, 2560 (2003).

[12] M. J. Twardos, P. E. Arratia, M. K. Rivera, G. A. Voth, J. P. Gollub, and R. E. Ecke, Phys. Rev. E **77**, 056315 (2008).

[13] D. Rothstein, E. Henry, and J. P. Gollub, Nature (London) **401**, 770 (1999).

[14] J. Gollub and D. Pine, Phys. Today **59**(8), 8 (2006).

[15] N. T. Ouellette and J. P. Gollub, Phys. Rev. Lett. **99**, 194502 (2007).

[16] N. T. Ouellette and J. P. Gollub, Phys. Fluids **20**, 064104 (2008).

[17] E. Hascoët, L. Rossi, and J. C. Vassilicos, in *Proceedings of the IUTAM Symposium on Flow Control and MEMS*, edited by J. F. Morrison, D. M. Birch, and P. Lavoie (Springer, New York, 2008).

[18] S. Lardeau, S. Ferrari, and L. Rossi, Phys. Fluids **20**, 127101 (2008).

[19] M. Priego and J. C. Vassilicos, Phys. Fluids **21**, 107101 (2009).

[20] J. Paret, D. Marteau, O. Paireau, and P. Tabeling, Phys. Fluids **9**, 3102 (1997).

[21] S. Ferrari and L. Rossi, Exp. Fluids **44**, 873 (2008).

[22] J. M. García de la Cruz, Ph.D. thesis, Imperial College London, 2011.

[23] L. Rossi, J. C. Vassilicos, and Y. Hardalupas, J. Fluid Mech. **558**, 207 (2006).

[24] J. Dávila and J. C. Vassilicos, Phys. Rev. Lett. **91**, 144501 (2003).

[25] V. Dallas, J. C. Vassilicos, and G. F. Hewitt, Phys. Rev. E **80**, 046306 (2009).

[26] J. F. Foss, Exp. Fluids **37**, 883 (2004).

[27] J. M. Ottino, *The Kinematics of Mixing: Stretching, Chaos, and Transport* (Cambridge University Press, Cambridge, UK, 1989).

[28] T. Faber and J. C. Vassilicos, Phys. Rev. E **82**, 026312 (2010).

[29] A. V. Wolf, *Aqueous Solutions and Body Fluids* (Harper and Row, New York, 1966).

[30] *Handbook of Chemistry and Physics : A Ready-Reference Book of Chemical and Physical Data*, 70th ed., edited by R. C. Weast (CRC Press, Boca Raton, FL, 1989).

[31] L. Rossi, S. Bocquet, S. Ferrari, J. M. Garcia de la Cruz, and S. Lardeau, Int. J. Heat Fluid Flow **30**, 505 (2009).

[32] M. Raffel, C. Willert, S. Wereley, and J. Kompenhans, *Particle Image Velocimetry* (Springer-Verlag, Berlin, 1998).

[33] L. Rossi, J. C. Vassilicos, and Y. Hardalupas, Phys. Fluids **19**, 078108 (2007).

[34] H. Tennekes, J. Fluid Mech. **67**, 561 (1975).